



K₃MB₅O₁₀ (M = Zn and Cd) with d¹⁰ configuration: Efficient and reusable catalysts for dehalogenation of halophenols

Xiaoyun Fan^{a,*}, Jing Liu^{a,1}, Kangrong Lai^{a,b}, Chuanyi Wang^{a,*}

^a Laboratory of Environmental Sciences and Technology, Xinjiang Technical Institute of Physics & Chemistry, and Key Laboratory of Functional Materials and Devices for Special Environments, Chinese Academy of Sciences, Urumqi 830011, China

^b Department of Physics, Changji University, Changji 831100, China

ARTICLE INFO

Article history:

Received 14 November 2016

Received in revised form

23 December 2016

Accepted 4 January 2017

Available online 6 January 2017

Keywords:

D¹⁰ configuration

Borate

Internal electric field

Dehalogenation

ABSTRACT

Two isostructural d¹⁰ configuration non-centrosymmetric materials: K₃ZnB₅O₁₀ (KZBO) and K₃CdB₅O₁₀ (KCBO) can act as efficient and reusable catalysts in the dehalogenation of halophenols. More than 90% of the 2, 4-DXP were degraded within 10 min with the dehalogenation efficiency 2, 4-DBP > 2, 4-DCP > 2, 4-DFP, the dehalogenation efficiency is almost 10 times higher than that of commercial P25 TiO₂ catalyst in the present reaction conditions. The internal electric field due to the distorted [MO₄] tetrahedral and [BO₃] units promote the charge separation in the initial process of photoexcitation and d¹⁰ configuration of Zn and Cd with large dispersion is useful for photoexcited electron transfers without recombination, thus enhance the photocatalytic activity. The dehalogenation pathways with KCBO outlined both oxidative and reductive dehalogenation. Our work is expected to offer new insight into photocatalytic theory for better understandings to photocatalytic reactions and rational design and synthesis of photocatalysts with high activity.

© 2017 Published by Elsevier B.V.

1. Introduction

Halophenols (XPs) represent one of the largest chemical classes of environmental contaminants and have great toxic effect on our ecosystem and health [1]. They are released to the environment via industrial discharge, accidental spills, and excessive usage of related products, and can also be formed during water disinfection or the pulp bleaching processes. XPs are generally resistant to biodegradation and difficult to remove from the environment, in particularly, the halogen atoms in XPs play a very crucial role in directing, substituting, and blocking some positions in the aromatic ring [2]. Therefore, the cleavage of the C-X (X = F, Cl, Br) bond is a critical step in the degradation process of XPs usually occurring at the first stage of reactions by which these compounds are degraded and detoxified [3]. Chlorophenols, such as 2-dichlorophenol, 2,4-dichlorophenol, 2,4,6-trichlorophenol, and pentachlorophenol are listed as priority pollutants and have perhaps received the most attention, as they are ubiquitous environmental contaminants. Bromophenols (BPs) usually found in high concentrations in sponges

and algae. Meanwhile, the rapidly increasingly levels of fluorinated organic pollutants in the environment has also been given much attention in recent decades. Conventional processes used for removal of XPs include physical, [4,5] chemical, [6–8] and biological methods [9]. However, these methods are limited by the toxicity of XPs to microbes or merely transfer the pollutants with the risk of secondary contamination.

Photocatalysis, which can be classified as an advanced oxidation method, is considered a promising technology for elimination of most organic contaminants in water. One of the most important problems limiting the applications to a great extent is the low photocatalytic activity caused by the photo-induced carrier recombination in semiconductor photocatalyst, which causes neutralization of the photo-induced electrons and holes before they can initiate the photocatalytic processes [10]. Although many approaches have been proposed and put into practice to solve this problem, the efficiency is still too low to separate electron-hole pairs completely during photocatalysis [11]. A photocatalyst particle with built-in electric field has been proposed to promote the separation of photo-induced charge carriers in recently. The existence of the built-in electric field provides a driving force which can easily transport the photo-induced charge carrier to the different directions, thus enhancing their separation and directly enhancing the photocatalytic performance [12,13].

* Corresponding authors.

E-mail addresses: xyfan@ms.xjb.ac.cn (X. Fan), cywan@ms.xjb.ac.cn, wangfu@ms.xjb.ac.cn (C. Wang).

¹ These authors contributed equally to this work.

Non-centrosymmetric materials can easily polarization which is the simplest way to obtain built-in electric field. [14] Thus, how to synthesize the polar structure efficiently remains a problem. Usually, there are three methods to obtain a non-centric structural materials. The first one is to direct borate-based noncentric materials by using π -conjugated planar borate rings; the second one is to acquire asymmetric building units by adopting transition metals existing second-order Jahn-Teller (SOJT) distortions; the third one is add to the polarization of structure by incorporating halide anions with large electronegativities [15]. According to the SOJT effect, the Jahn-Teller distortion can occur in Zn^{2+} and Cd^{2+} with fully occupied d -orbitals, which is favorable for the formation of the non-centrosymmetric structure [16]. And the conduction bands of d^{10} metal cations consist of sp orbitals which are dispersed well resulting in high mobility of photogenerated electrons [17]. Moreover, the flexible coordination of the Zn and Cd tetrahedra makes borate anion framework much variable. Therefore incorporation of borates with asymmetric π systems and d^{10} metal cations is an eminent strategy to prepare catalysts with high photoactivity. [18]

Herein, we demonstrate that two isostructural d^{10} configuration non-centrosymmetric materials by introducing alkali K metal atoms with a large radius into the borate system, KZBO and KCBO, which can function as effective photocatalysts for dehalogenation of XPs under UV light irradiation. More than 90% of the 2, 4-DXP were degraded within 10 min with the dehalogenation efficiency 2, 4-DBP > 2, 4-DCP > 2, 4-DFP, which is closely related to the physical properties of 2, 4-DXP, and approximately 82.50% of the fluoride content, 90.50% of the chloride content, and 95.75% of the bromide content was converted into F^- , Cl^- , and Br^- anions by KCBO, while the conversion percentage for KZBO is 80.25%, 83.11% and 89.77%. The distorted $[\text{MO}_4]$ tetrahedral and $[\text{BO}_3]$ units are responsible for the formation of the non-centrosymmetric structure, which facilitates producing an internal electric field that can provide a driving force for the separation of photogenerated electrons and holes and d^{10} configuration of Zn and Cd with large dispersion is useful for photoexcited electron transfers without recombination, thus enhance the photocatalytic activity. The dehalogenation pathways with KCBO outlined both oxidative and reductive dehalogenation.

2. Experimental

Materials. 2,4-difluorophenol (2,4-DFP), 2,4-dichlorophenol (2,4-DCP), 2,4-dibromophenol (2,4-DBP), and terephthalic acid (TA) were purchased from Sinopharm Chemical Reagent Co., Ltd. K_2CO_3 , KNO_3 , ZnO , CdO , Na_2SO_4 , and H_3BO_3 were obtained from Tianjin Chemicals, Inc. Methanol and acetonitrile were chromatographic grade (Sinopharm Chemical Reagent Co., Ltd). Deionized water was used throughout this study.

Synthesis of KMBO. KZBO powder were prepared by employing a conventional solid-state reaction method with a stoichiometric mixture of K_2CO_3 , ZnO and H_3BO_3 . After grounded in an agate mortar and packed into crucible, the raw materials were heated to 400°C , held for 12 h and at 600°C for 48 h. Under the same condition, a stoichiometric mixture of KNO_3 , CdO and H_3BO_3 were prepared for the synthesis of KCBO powder.

Characterization. X-ray diffraction (XRD) patterns of the samples were recorded by a Bruker D8 Advance X-ray diffractometer equipped with a diffracted-beam monochromator set for Cu $\text{K}\alpha$ radiation ($\lambda = 1.5418 \text{ \AA}$). The morphologies of KMBO were observed on a scanning electron microscope (SEM) using a ZEISS SUPRA55VP apparatus and the energy dispersive X-ray spectroscopy (EDX) were obtained by the EDX8000. The diffuse reflectance absorption spectra (DRS) were recorded in the range from 200 to 800 nm using a Solidspec-3700 DUV spectrometer with BaSO_4 as a reference. The Brunauer-Emmett-Teller (BET) surface area was obtained

from the N_2 adsorption/desorption isotherms recorded at 77 K (QUADRASORB IQ, Quantachrome Instrument Corp.). High performance liquid chromatography (HPLC) (Ultimate 3000, Dionex) were carried out with a C18 column ($4.6 \text{ mm} \times 250 \text{ mm}$). The size of the sample loop was $20 \mu\text{L}$. For XPs, a mixture of methanol and water [85/15 (v/v)] was used as an effluent with the flow rate 1 mL/min , detector wavelength 273 nm , 282 nm , and 285 nm for 2,4-DFP, 2, 4-DCP, and 2, 4-DBP, respectively. The intermediate products during 2, 4-DXP degradation were qualitatively analyzed by a liquid chromatography-mass spectrometry (LC-MS, Agilent 1290). Ion chromatography (IC) was measured by the ICS 5000. The photocurrents of UV light on and off studies were determined on a CHI660E electrochemical system using a standard three-electrode cell with a working electrode ($10 \text{ mm} \times 10 \text{ mm}$), a platinum plate as the counter electrode, and a standard calomel electrode (SCE) as the reference electrode. The KMBO film was prepared on ITO glass, followed by air-drying. The experiments were performed in a 50 mL quartz cylinder reactor which was placed in front of a 500 W mercury lamp ($\lambda > 254 \text{ nm}$; Perfect Light Company, Beijing, China). The photoelectron chemical (PEC) activities of the samples were all evaluated in a 0.1 M Na_2SO_4 solution. Atomic force microscopy (AFM) combined with Kelvin probe force microscopy (KPFM) measurements were performed with an atomic force microscope (Bruker Multimode 8). Images were obtained in tapping mode with a scan rate of 1 Hz and an AC mode for a scan size of $1 \mu\text{m} \times 1 \mu\text{m}$. In the experiment, KMBO nanoparticles were first dispersed in water and then sprayed on a Pt substrate to form a film. The sample was baked in a dry oven at 600°C for 4 h. For the light irradiation experiment, a mercury lamp and a convex lens with a focusing spot size (d) of 1.5 cm were used to introduce focused UV light onto the measurement region between the tip of the atomic force microscope and sample. Fluorescence spectra were measured on a Hitachi fluorescence spectrophotometer F-7000. The $\cdot\text{OH}$ radical trapping experiments were carried out using the following procedure: terephthalic acid (TA) (8.3 mg) was first dissolved in 100 mL of dilute NaOH solution ($2 \times 10^{-3} \text{ M}$), followed by addition of 50 mg of photocatalysts, and stirred for 20 min in dark. The suspension was irradiated by a 500 W mercury lamp. The fluorescence emission spectrum (excited at 312 nm) of the solution was measured every 2 min during irradiation.

Photocatalytic Activity. Typically, 50 mg catalysts was added into 100 mL aqueous solution of XPs (50 mg/L) (2, 4-DFP, 2, 4-DCP, and 2, 4-DBP) in a 250 mL glass beaker, then stirred for 20 min in the dark to attain adsorption equilibrium, and irradiated by a 500 W mercury lamp (the light intensity at the test samples $= 0.287 \text{ W/cm}^2$). The percentage of residual contaminants solution at a selected time of irradiation is given by C/C_0 , where C_0 is the concentration of the contaminants solution at the initial stage, and C is the concentration at selected irradiation times. To test the reproducibility and uncertainty of the degradation experiments, the photochemical reactions were repeated three times.

3. Results and discussion

The as-prepared samples crystallize in the monoclinic system with space group $P2_1/n$ [19,20] and cell parameters, $a = 7.6391(5) \text{ \AA}$, $b = 19.2304(13) \text{ \AA}$, $c = 7.6905(5) \text{ \AA}$. The structure exhibits a three-dimensional (3D) network, consisting of ZnO_4 , KO_n ($n = 7, 8$) distorted polyhedra, and isolated B_5O_{10} units. The Zn atoms are coordinated to four O atoms. The ZnO_4 tetrahedra are isolated; they connect each other by sharing the B_5O_{10} group. (Fig. 1). The morphology also be investigated, which shows a unregularly shape (Fig. S1) with $0.951 \text{ m}^2/\text{g}$ [18] and $1.54 \text{ m}^2/\text{g}$ BET surface areas for KZBO and KCBO, respectively (Fig. S2).

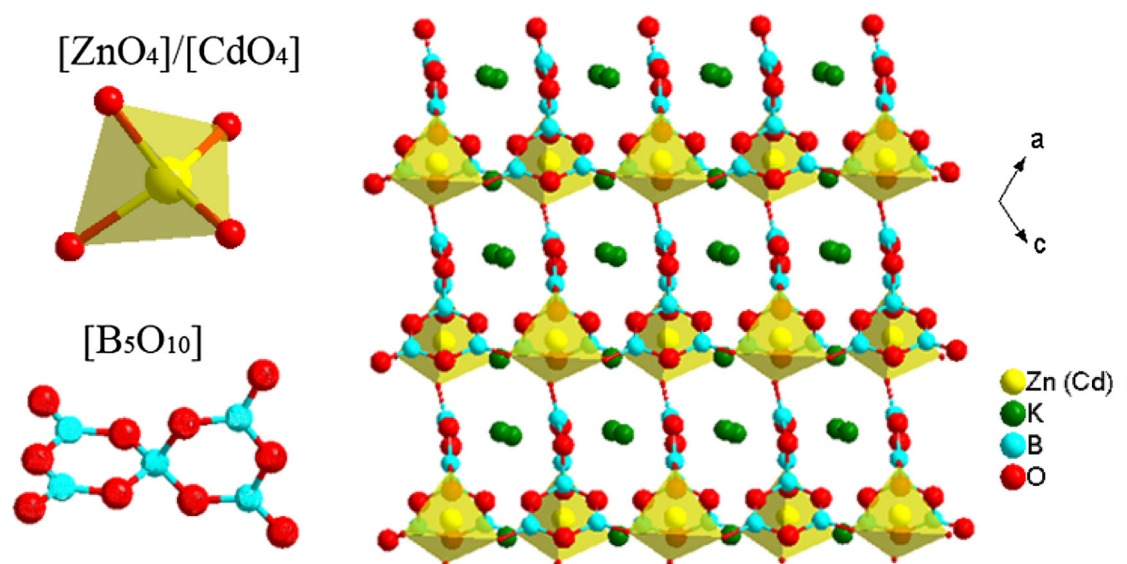


Fig. 1. Drawing of the structure of KMBO viewed down the *b*-axis.

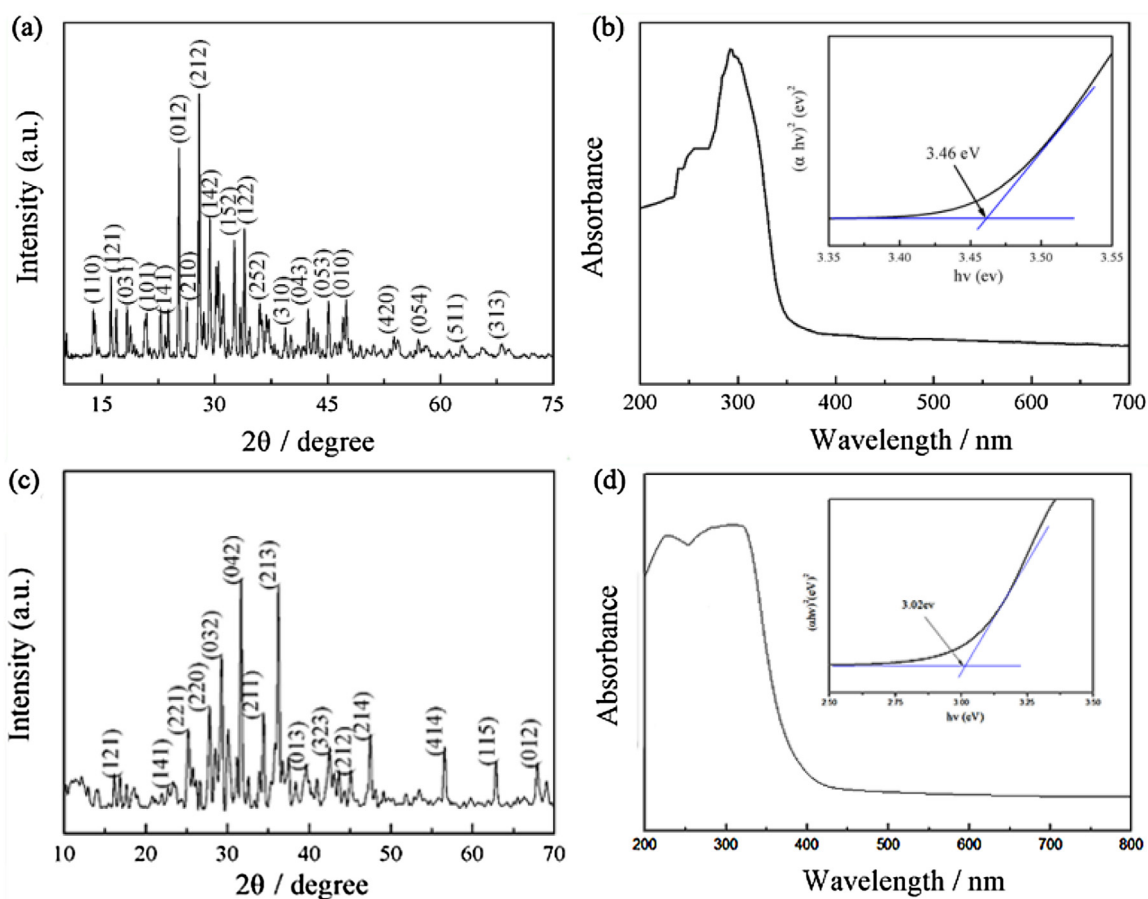


Fig. 2. XRD pattern (a) and (c) and UV-vis diffusive reflectance spectrum (b) and (d) for KCBO and KZBO, respectively. Inset of (b) and (d): Plots of $(\alpha \times h\nu)^2$ versus energy ($h\nu$) for the samples.

The crystal structure of KZBO and KCBO was confirmed by XRD analysis. As shown in Fig. 2(a), all the XRD peaks are indexed to monoclinic KCBO. The presence of elements and atomic percentages confirm that the as-prepared samples are of KCBO. KCBO performed a 360 nm absorption band-edge in the UV region

(Fig. 2(b)), while KZBO performed a 405 nm absorption band-edge in the visible region as reported in our previous work [18].

The photocatalytic activity of KMBO were evaluated by the dehalogenation of XPs under UV light irradiation. As shown in Fig. 3, prior to the illumination, the suspension was magnetically stirred in the dark condition for 20 min in order to attain the adsorption-

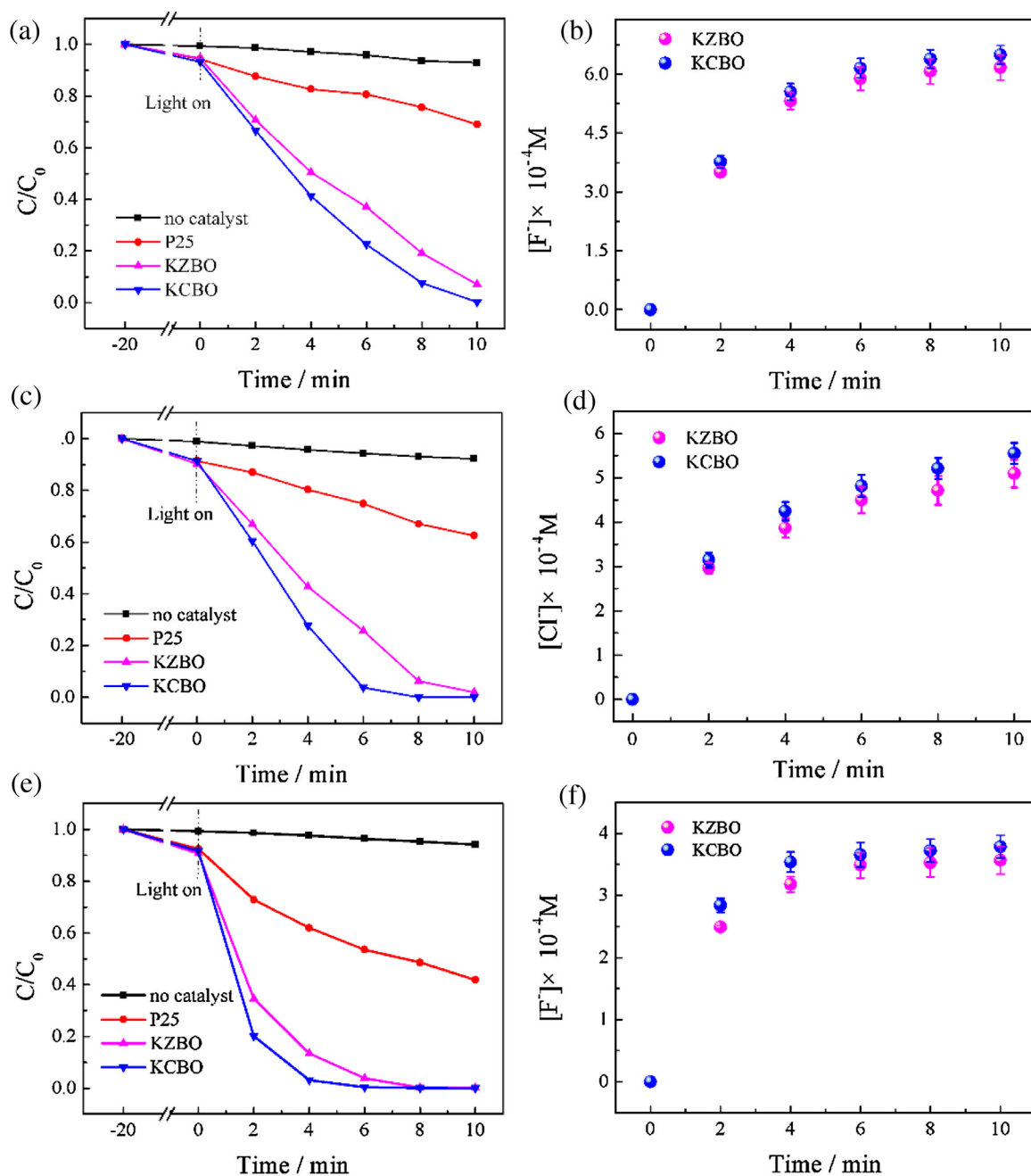


Fig. 3. Photodehalogenation of (a) 2, 4-DFP, (c) 2, 4-DCP, and (e) 2, 4-DBP in aqueous dispersions and formation of (b) F^- , (d) Cl^- , (f) Br^- as a function of irradiation time during the photodehalogenation process under UV light.

Table 1
Dehalogenation of HPs in aqueous dispersions by KZBO and KCBO powders.

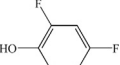
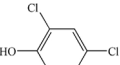
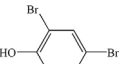
Reactant	Time/min	HPs Removal		Halide Ion Released	
		KZBO	KCBO	KZBO	KCBO
	10	90.53%	97.64%	80.25%	84.50%
	10	100%	100%	83.11%	90.50%
	10	100%	100%	89.77%	95.34%

Table 2Comparison of chlorophenol degradation performances for modified TiO₂ photocatalyst and the present powders.

Photocatalyst	Conditions			Efficiency		References
	Dosage(g/L)	illumination	model compounds and content	Time	degradation	
KZBO	0.05	$\lambda > 254$ nm	2,4- DCP, 30 mmol	10 min	83%	This work
KCBO	0.05	$\lambda > 254$ nm	2,4- DCP, 30 mmol	10 min	90%	This work
pure TiO ₂	0.25	$\lambda > 400$ nm	4- CP, 2 mmol	8 h	15%	[22]
Ni ₂ O ₃ /TiO _{2-x} B _x	1.0	$\lambda > 400$ nm	TCP, 5 mmol	4 h	80%	[23]
Au- TiO ₂	1.0	700 nm $> \lambda > 460$ nm	4-CP, 0.4 umol	180 min	25%	[24]
Pt ^{II} -TiO ₂	1.0	$\lambda > 420$ nm	4-CP, 12.5 mmol	180 min	80%	[25]
Fe ₂ O ₃ /TiO ₂	1.0	sunlight	4-CP, 77.5 mmol	180 min	100%	[26]
Pt-Borate- TiO ₂	1.0	$\lambda > 320$ nm	2,4- DCP, 15 mmol	90 min	95%	[27]
(CaO, MgO, SrO)- TiO ₂	2.0	578 nm $> \lambda > 303$ nm	4- CP, 9 mmol	60 min	100%	[28]
(B, N)- TiO ₂	0.25	$\lambda > 400$ nm	4- CP, 2 mmol	8 h	78%	[29]
N/Sn-TiO ₂	0.25	$\lambda > 400$ nm	4- CP, 2 mmol	8 h	49%	[22]

deposition equilibrium and about 10% of 2, 4-DXP were adsorbed onto KMBO. More than 90% of the 2, 4-DXP were degraded within 10 min with photodegradation rates decreasing in the order: 2, 4-DBP $>$ 2, 4-DCP $>$ 2, 4-DFP and approximately 82.50% of the fluoride content, 90.50% of the chloride content, and 95.75% of the bromide content was converted into F⁻, Cl⁻, and Br⁻ anions, respectively, while the conversion percentage for KZBO is 80.25%, 83.11% and 89.77% (Table 1). Photodegradation rates strongly correlates with the bond energy of C–X bond. Average bond enthalpies of C–F, C–Cl, and C–Br bonds are 485, 327, 285 kJ/mol, respectively. This close relationship explains the reason for different reaction kinetics due to halogen atoms [21]. The C–F bonds are stronger than other carbon-halogen bonds and that defluorination is less exothermic than other dehalogenation reactions, making fluorinated aromatics more resistant to both biotic and abiotic degradation [8]. In addition, the smaller size of the halogen atom also lead to in decreased steric effects and increased electrostatic effects, which are responsible for a significantly greater variation in bond strengths and result in greater selectivity in the degradation. The present photocatalyst could achieve the overall halophenols removal of 83% and this value is higher than most of results reported in the literatures [22–29] as shown in Table 2.

As for an excellent photocatalytic material, possessing a stable photocatalytic performance is very important. To investigate the performance stability of the KCBO photocatalyst, we carried out three-cycle photocatalytic experiments for 2, 4-DFP decomposition, and the corresponding results are shown in (Fig. S3(b)). After three successive cycles, while the photocatalytic activity of the KCBO samples was effectively maintained except for 2% decrease after cycling reactions. Hence, KCBO photocatalysts display the splendid stability during the photocatalytic process (Fig. S4(a)). To further understand the stability of the samples, XRD patterns before and after three cycles defluorination reaction further indicating the stability of the KCBO samples. Altogether, the KCBO sample show good stability.

The dipole moment is known to induce the formation of local fields in the interior of the distorted polyhedra, which is useful to promote the separation of electron-hole pairs in semiconductor materials as demonstrated by Inoue et al. [30] Hence, a bond valence approach [31] was adopted to evaluate the local dipole moments listed in Table 3. The calculations showed that the [MO₄] tetrahedra were so heavily distorted that the center of the gravity deviated from the position of the M²⁺ ion, generating dipole moments in the tetrahedra unit with the values 1.7054 D and 3.0012 D for [ZnO₄] and [CdO₄], respectively. In addition, as shown in Fig. 4, each [MO₄] tetrahedron shares its four oxygen atoms with four [BO₃] units, which influences the polarization of [BO₃] and likely affects the electronic structure. From the bond dipole moments of [BO_n] (n = 3, 4) and [MO₄] units, it is found that KZBO and KCBO possess an electric polarization along the *c*-axis direc-

Table 3Dipole Moments of BO_n (n = 3 or 4), and MO₄ (M = Zn or Cd) polyhedras in KMBO.

KZBO		KCBO	
Polyhedral unit	Dipole Moment/debye	Polyhedral unit	Dipole Moment/debye
ZnO ₄	1.7054	CdO ₄	3.0012
B(1)O ₃	0.9419	B(1)O ₃	1.1608
B(3)O ₃	0.9675	B(2)O ₃	1.1346
B(2)O ₄	0.2842	B(3)O ₄	0.4941
B(4)O ₃	0.9157	B(4)O ₃	1.2676
B(5)O ₃	0.5512	B(5)O ₃	0.7358

tion with net dipole moment 5.3659 D and 7.7941 D, respectively. The larger polarization ability of KCBO leads to higher efficiency of charge separation, which is the most significant factor that deteriorate the photoactivity of semiconductor catalyst. The result is in good agreement with the photocatalytic activity result.

To gain insight into a probable reason for this excellent photocatalytic property of KCBO, we examine its electronic band structure determined from density functional calculations, which is presented in terms of the density of states (DOS) plots in Fig. 5(a) and (b). Fig. 5(a) shows the quasiparticle band structure for KCBO. Similar to most semiconductor, the top of valence band is dominated by O 2p orbitals and the conduction band (CB) is mainly composed of Cd 4p, O 2p and B 2p contributions. Furthermore, the shallow and fully occupied 4d orbitals in KCBO compounds with Cd²⁺ cation electronic configurations (4d¹⁰) strongly hybridize with these oxygen states; this behavior pushes up the valence band maximum and reduces the band gap. Another character of these band structures is the large band dispersions, derived mainly from the Cd 4p orbitals, at the bottom of conduction band located at the point, indicating light electron band masses and potentially high electron mobility. There are three types of oxygen atoms in KCBO: the O1 atoms belong to CdO₄ unit, while the O2 and the O3 atoms belong to the two rings of [B₅O₁₀] unit as shown in Fig. 5(c). The VB top has O 2p contributions, and O1, O2 and O3 atoms have similar contribution values. Therefore, photoexcitation from the VB top to the CB generates holes at the O 2p states in all O atoms. (Fig. 5(b)) As a result, the electron carriers in KCBO should have a higher mobility and longer diffusion length, which would significantly enhance the electron-hole pair separation and carrier transport from the bulk of the sample to surface. KCBO is found to possess a nonzero electric polarization along the *b*-axis direction, as expected from the fact that it belongs to the space group of *P21/n* (Fig. 5(c)). As expected the internal polar field provides a driving force for the photoexcited holes and electrons to move to their respective reduction and oxidation sites. Local probe techniques allow for direct observation of not only the spatially resolved surface properties, but also the local manifestation of physical/chemical characteristics in nanostructures [32–35].

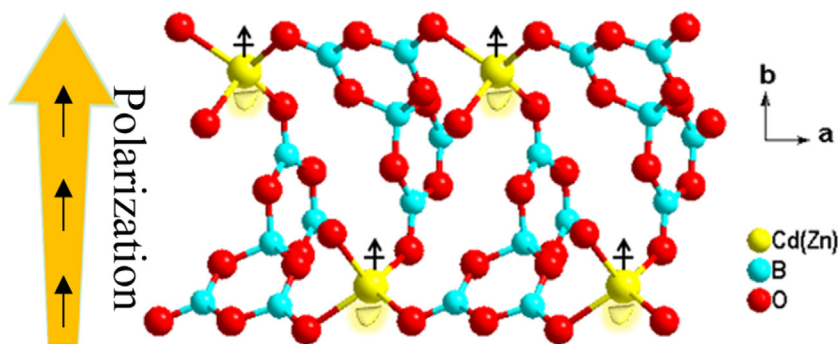


Fig. 4. Crystal structures $[MB_5O_{10}]$ ($M = Zn$ and Cd) units.

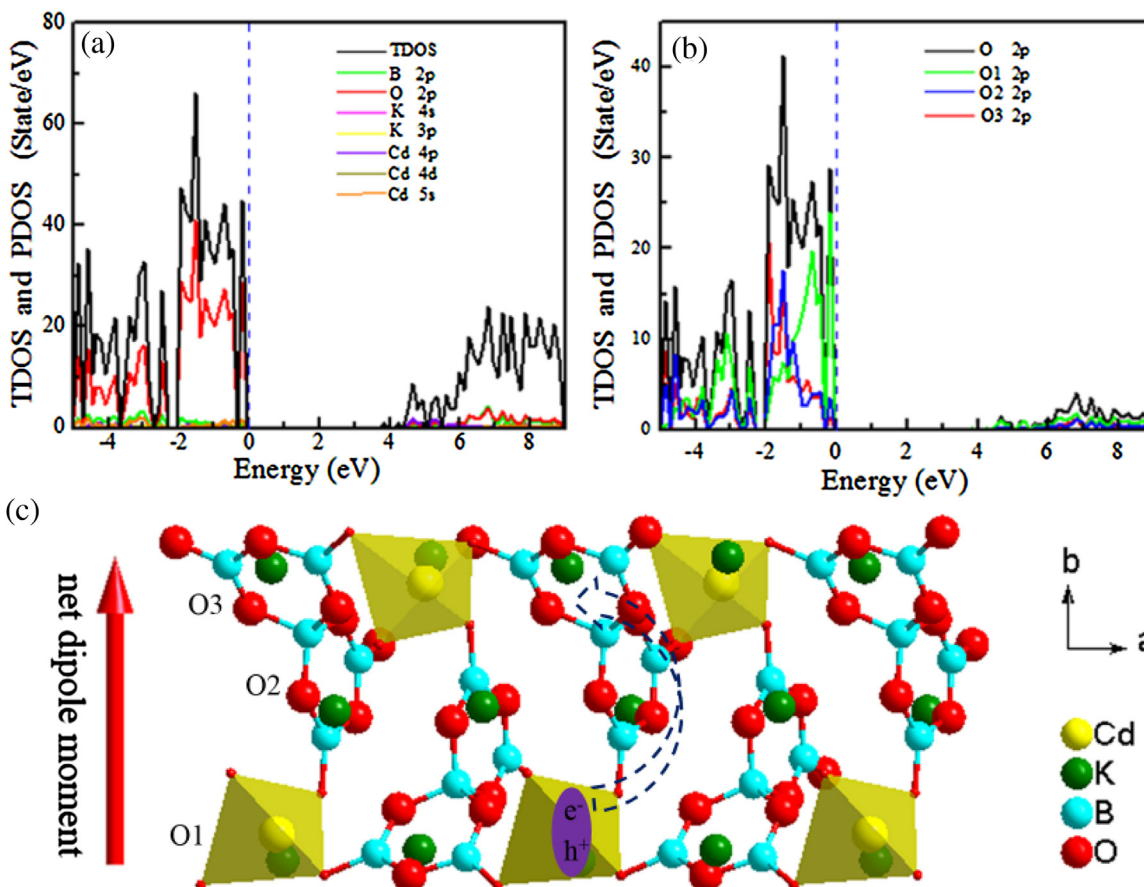


Fig. 5. The total and projected DOS plots calculated for (a) KCBO and (b) the different O atoms in KCBO. (c) A schematic illustration showing the internal polarized field enhances the charge separation and the photocatalytic mechanism of KCBO.

To further investigate the optoelectronic properties of the KMBO samples, a variety of Kelvin probe force microscopy (KPFM) experiments were performed. A Kelvin probe measures the work function difference between a sample and a metallic probe, which is called the contact potential difference (CPD). The sign definition is taken such that the CPD increases with increasing sample work function. The surface photovoltage (SPV) is defined as the illumination-induced change in the surface potential, by mapping the surface potential distribution, the charge separation was characterized by KPFM measurement [36]. When illumination the sample with a white light source, the surface potential changes dramatically whereas the atomic force microscopy (AFM) topography signal remains unaffected (Fig. 6(a)). The KPFM image in darkness (Fig. 6(b)) shows greater contrast with respect to the potential

more negative with respect to under illumination (Fig. 6(c)). The contrast enhancement in the KPFM image unambiguously demonstrates that photogenerated excitons are split at the interface between the two domains, leading to the accumulation of electrons in the one domains and holes in the other domains. The average values of the surface potential in dark along the blue line ($A'B'$) is -4.995 V, while under illumination is (line $A''B''$) -5.012 V, thus, the difference between the average values of the surface potential of the two phases decreases around 17 mV (Fig. 6(d)). A negative shift is expected due to exciton splitting and donor-to-acceptor electron transfer. When the sample is under illumination, the excess carrier accumulation leads to a change in surface potential compared to the dark state. It can be concluded that due to the charge pairs transferred and accumulated to opposite directions thus would cause

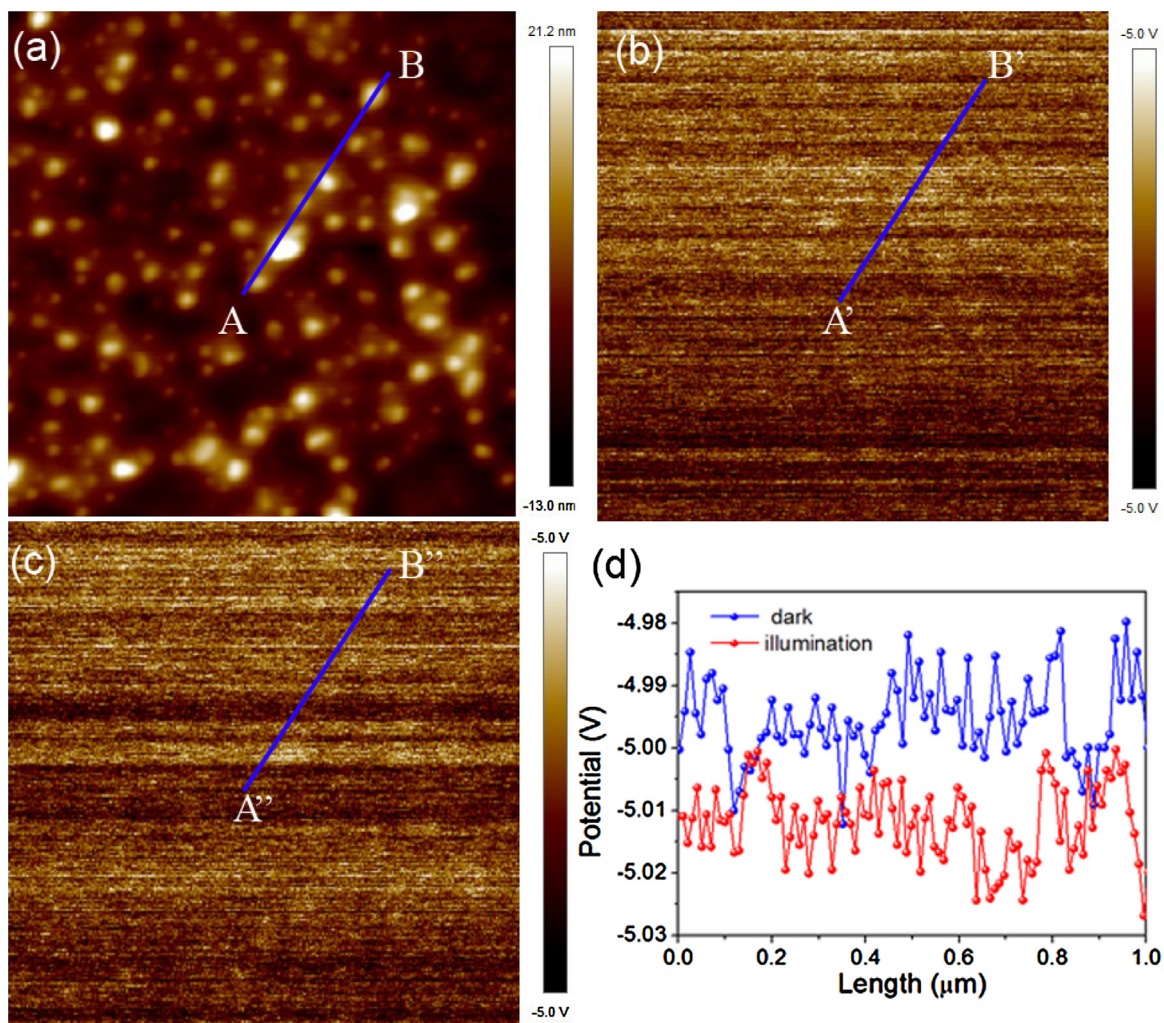


Fig. 6. AFM, KPFM imaging and surface potential analysis for KCBO: (a) topographic images, and corresponding surface potential images (b) in dark and (c) under illumination; (d) Surface potential profile along the blue line in (b) and (c). (For interpretation of the references to colour in this figure legend, the reader is referred to the web version of this article.)

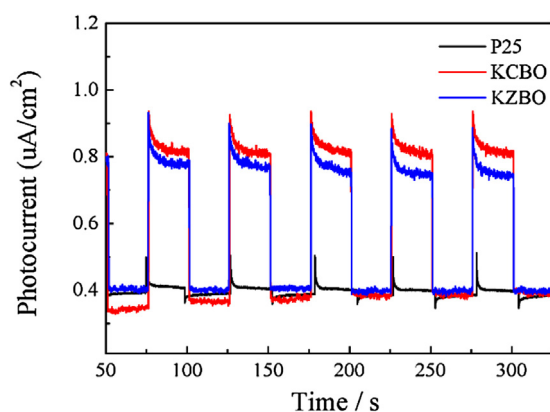


Fig. 7. Photocurrent spectra of KMBO and P25 TiO₂.

the potential difference between different states, this would finally separate the photogenerated excitons [37].

In order to further confirm that the photon-to-electron conversion efficiency of the KMBO particles, PEC photocurrent were measured on a photoelectrochemical test device fabricated by drop-casting the material dispersed in ethanol (0.03 g/mL) onto indium-doped tin oxide (ITO) coated glass. The Fig. 7 shows the

transient photocurrent response versus time of P25 and KMBO photocatalyst via several on-off cycles. It is found that the photocurrent of the KMBO photocatalyst is much higher than P25. The photoresponses of P25 electrode showed weak photocurrent response relative to KMBO. The photocurrent of KMBO under UV light irradiation can be enhanced by 10 for KCdBO and 9 times for KZnBO, implying an enhanced separation efficiency of photoinduced electrons and holes. All the samples exhibit excellent switching behavior. The photocurrent response of the KMBO material is reasonably reversible and stable, from which we can see that the current can reproducibly increase severely under each irradiation and quickly recover in the dark.

2, 4-DBP were selected as a model compound to explore the dehalogenation pathway of XPs. The intermediate products resulting from 2, 4-DBP photocatalytic degradation were analyzed using LC-MS depicted in Fig. S4 and Table S1. According to the previously proposed mechanisms for degradation of other aromatic organic molecules [38,39] and the experimental results in this study, the photodegradation pathway of 2, 4-DBP was proposed in Scheme S1, which outlined both oxidative and reductive debromination. On one hand, the holes generated on KCBO by UV light irradiation react with adsorbed water to form hydroxyl radicals ($\cdot\text{OH}$) or directly oxidize surface 2, 4-DBP and a part of the generated-electrons react with the dissolved oxygen to form ($\cdot\text{O}_2^-$), which further gener-

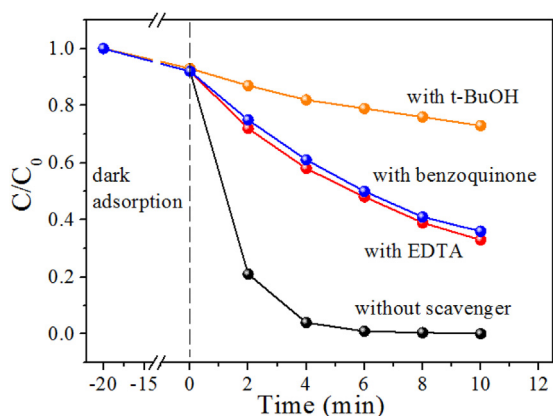


Fig. 8. Photocatalytic degradation of 2, 4-DBP with the addition of hole and radical scavenger under UV light irradiation.

ated ($\cdot\text{OH}$) to accelerate the oxidation reaction of 2, 4-DBP. On the other hand, 2, 4-DBP can undergo reductive debromination to produce less-brominated homologues first and then reacts with ($\cdot\text{OH}$), leading to the formation of phenol.

To investigate the reactive species of KZBO photocatalysts in the photocatalytic mechanism, a series of scavengers was used during the degradation of 2, 4-DBP photochemical reaction process [40]. Fig. 8 shows the results in the presence of the selected scavengers. In this study, EDTA was scavenger of holes (h^+), benzoquinone (BQ) was added as a superoxide ions ($\cdot\text{O}_2^-$) scavenger, and *t*-BuOH was used as a hydroxyl radical ($\cdot\text{OH}$) scavenger, respectively [41]. It is evident that no scavengers the degradation rate is >99.5%. However, in the presence of EDTA and benzoquinone (BQ), the decrease of the rate are similar to each other, 64.4% and 67.7%, respectively. When in the presence of *t*-BuOH, the degradation rate is 27.1%. Based on these results, it can be concluded that the ($\cdot\text{OH}$) is the important role and the (h^+) and ($\cdot\text{O}_2^-$) play acted a secondary role in the photocatalytic degradation [42]. Although 2, 4-DBP cannot be completely debromination by KCBO, the degradation intermediates as well as end products are less toxic than that of 2, 4-DBP and can be readily biodegraded into harmless compounds by microorganisms under both aerobic and anaerobic conditions.

An additional experiment was also performed to examine the capability of light-excited KCBO to induce the formation of hydroxyl radicals, which is the key reactive species in the degradation of organic compounds [43]. It is well-known that TA can capture ($\cdot\text{OH}$) and form 2-hydroxyterephthalic acid which can be easily detected by its fluorescence signal. Fig. S5 shows fluorescence spectra observed for the KCBO suspension containing TA irradiated for various exposure times. The fluorescence intensity increases linearly with irradiation time (inset of Fig. S6). This result is a strong indication that the photogenerated charge carriers in KCBO possess strong redox ability, and are long-lived enough to react with H_2O and hydroxyl groups adsorbed on the catalyst surface to form the desirable ($\cdot\text{OH}$) radical species.

Overall, the noncentric-symmetric nature of these crystal structure is responsible for their unique catalytic properties. It can be concluded that the internal electric field of a nonlinear structure shows a spontaneous polarization which behave as an internal (*p-n*) junction which largely determines the band bending at the interface and the surface where the mobile carriers can accumulate and to a large extent also determines the photochemistry properties. [44] Fig. 9 shows that in a noncentric-symmetric structure material, the depolarizing fields screen the surface charge by drawing electrons to the positive (C^+) face which resulting in downward band bending. And meantime, driving the holes to the negative (C^-) face, leading to upward bending at the (C^-) face. In such situation, the

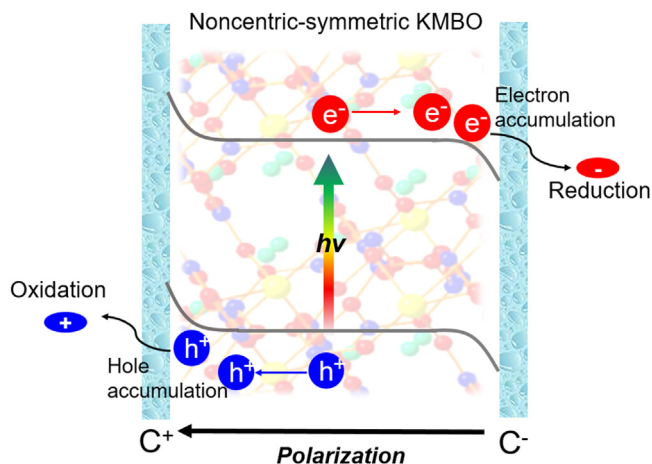


Fig. 9. Schematic illustration of a noncentric-symmetric structured KMBO photocatalyst.

photo-induced charges are driven toward opposite locations and produce oxidation and reduction products.

4. Conclusion

In summary, we have fabricated two isostructural non-centrosymmetric materials- $\text{K}_3\text{ZnB}_5\text{O}_{10}$ (KZBO) and $\text{K}_3\text{CdB}_5\text{O}_{10}$ (KCBO). Moreover, the stable and higher photocatalytic performance over KMBO for the degradation of 2, 4-DXP has been developed. More than 90% of the 2, 4-DXP were dehalogenation by KMBO samples within 10 min under the UV light irradiation. The $[\text{MO}_4]$ and the $[\text{BO}_3]$ units are responsible for the formation of the non-centrosymmetric structure, moreover, d^{10} configuration of Zn and Cd with large dispersion are useful for photo-excited electron transfers. The larger polarization ability of KCBO is responsible for the higher dechlorination efficiency, which facilitates producing an internal electric field that provides a driving force for the separation of photo-generated electrons and holes which leading to a restraining of the recombination of the electron-hole pair and finally promoting the migration efficiency of photogenerated electron-hole on the interface. Compared with traditional photocatalytic process, the present studied process showed promising dehalogenation efficiency. We hope that this approach of targeted design can be harnessed to discover other new photo active materials with higher efficiencies of separation of photo-generated electrons and holes. We next will focus on the reaction process between the pollutant molecules and the semiconductor interface, so that can fully understand the reason why such material has so high efficiency for the degradation of XPs.

Acknowledgements

This work was supported by National Nature Science Foundation of China (Grant No. 21473248), the CAS Youth Innovation Promotion Association (2017473), Natural Science Foundation of Xinjiang Uygur Autonomous Region (Grant Nos. 2016D01A072, the “Western Light” Program (Grant No. YBXM 201401) of Chinese Academy of Sciences.

Appendix A. Supplementary data

Supplementary data associated with this article can be found, in the online version, at <http://dx.doi.org/10.1016/j.apcatb.2017.01.016>.

References

- [1] H.M. Hwang, R.E. Hodson, Degradation of phenol and chlorophenols by sunlight and microbes in estuarine water, *Environ. Sci. Technol.* 20 (1986) 1002–1007.
- [2] A.K. Patra, A. Dutta, A. Bhaumik, Highly ordered mesoporous $\text{TiO}_2\text{-Fe}_2\text{O}_3$ mixed oxide synthesized by sol-gel pathway: an efficient and reusable heterogeneous catalyst for dehalogenation reaction, *ACS Appl. Mater. Inter.* 4 (2012) 5022–5028.
- [3] H. Rong, S. Cai, Z. Niu, Y. Li, Composition-dependent catalytic activity of bimetallic nanocrystals: AgPd -catalyzed hydrodechlorination of 4-chlorophenol, *ACS Catal.* 3 (2013) 1560–1563.
- [4] J. Guo, J. Guo, Z. Xu, Recycling of non-metallic fractions from waste printed circuit boards: a review, *J. Hazard. Mater.* 168 (2009) 567–590.
- [5] J.F. Quensen, S.A. Muller, M.K. Jain, J.M. Tiedje, Reductive dechlorination of DDE to DDMU in marine sediment microcosms, *Science* 280 (1998) 722–724.
- [6] G.K. Parshetti, R.A. Doong, Synergistic effect of nickel ions on the coupled dechlorination of trichloroethylene and 2,4-dichlorophenol by Fe/TiO_2 nanocomposites in the presence of UV light under anoxic conditions, *Water Res.* 45 (2011) 4198–4210.
- [7] D. Sadowsky, K. McNeill, C.J. Cramer, Dehalogenation of aromatics by nucleophilic aromatic substitution, *Environ. Sci. Technol.* 48 (2014) 10904–10911.
- [8] D. Sadowsky, K. McNeill, C.J. Cramer, Thermochemical factors affecting the dehalogenation of aromatics, *Environ. Sci. Technol.* 47 (2013) 14194–14203.
- [9] P.H. Howard, D.C. Muir, Identifying new persistent and bioaccumulative organics among chemicals in commerce. III: byproducts, impurities, and transformation products, *Environ. Sci. Technol.* 47 (2013) 5259–5266.
- [10] Y.Q. Qu, X.F. Duan, Progress, challenge and perspective of heterogeneous photocatalysts, *Chem. Soc. Rev.* 42 (2013) 2568–2580.
- [11] H. Huang, X. Li, J. Wang, F. Dong, P.K. Chu, T. Zhang, Y. Zhang, Anionic group self-doping as a promising strategy: band-gap engineering and multi-functional applications of high-performance CO_3^{2-} -Doped $\text{Bi}_2\text{O}_3\text{CO}_3$, *ACS Catal.* 5 (2015) 4094–4103.
- [12] Y. Cui, J. Briscoe, S. Dunn, Effect of ferroelectricity on solar-light-driven photocatalytic activity of BaTiO_3 -influence on the carrier separation and stern layer formation, *Chem. Mater.* 25 (2013) 4215–4223.
- [13] M.M. Kukulja, R.V. Tsyshkevsky, O. Sharia, Effect of polar surfaces on decomposition of molecular materials, *J. Am. Chem. Soc.* 136 (2014) 13289–13302.
- [14] L. Li, P.A. Salvador, G.S. Rohrer, Photocatalysts with internal electric fields, *Nanoscale* 6 (2014) 24–42.
- [15] H. Yu, H. Wu, Q. Jing, Z. Yang, P.S. Halasyamani, S. Pan, Polar polymorphism: α -, β -, and γ - $\text{Pb}_2\text{Ba}_4\text{Zn}_4\text{B}_{14}\text{O}_{31}$ -synthesis, characterization, and nonlinear optical properties, *Chem. Mater.* 27 (2015) 4779–4788.
- [16] B.P. Yang, C.L. Hu, X. Xu, C. Huang, J.G. Mao, $\text{Zn}_2(\text{VO}_4)(\text{IO}_3)$: a novel polar zinc(II) vanadium(V) iodate with a large SHG response, *Inorg. Chem.* 52 (2013) 5378–5384.
- [17] H.L. Jiang, F. Kong, Y. Fan, J.G. Mao, ZnVSe_2O_7 and $\text{Cd}_6\text{V}_2\text{Se}_5\text{O}_{21}$: new d^{10} transition-metal selenites with V(IV) or V(V) cations, *Inorg. Chem.* 47 (2008) 7430–7437.
- [18] J. Liu, X. Fan, Y. Zhu, J. Zhao, F. Jiang, S. Chen, H. Sun, J. Xu, W. Deng, C. Wang, Efficient photodechlorination of chlorophenols on polarized $\text{MZnB}_5\text{O}_{10}$ ($\text{M} = \text{Na}$ and K) nonlinear optical materials, *Appl. Catal. B: Environ.* 181 (2016) 436–444.
- [19] H. Wu, S. Pan, H. Yu, Z. Chen, F. Zhang, Synthesis, crystal structure and properties of a new congruently melting compound $\text{K}_3\text{ZnB}_5\text{O}_{10}$, *Solid State Sci.* 14 (2012) 936–940.
- [20] H. Yu, S. Pan, H. Wu, J. Han, X. Dong, Z. Zhou, Synthesis, structure characterization and optical properties of a new tripotassium cadmium pentaborate $\text{K}_3\text{CdB}_5\text{O}_{10}$, *Solid State Sci.* 184 (2011) 1644–1648.
- [21] Y. Hwang, A. Salatas, P.D. Mines, M.H. Jakobsen, H.R. Andersen, Graduated characterization method using a multi-well microplate for reducing reactivity of nanoscale zero valent iron materials, *Appl. Catal. B Environ.* 181 (2016) 314–320.
- [22] E. Wang, T. He, L. Zhao, Y. Chen, Y. Cao, Improved visible light photocatalytic activity of titania doped with tin and nitrogen, *J. Mater. Chem.* 21 (2011) 144–150.
- [23] W. Zhao, W. Ma, C. Chen, J. Zhao, Z. Shuai, Efficient degradation of toxic organic pollutants with $\text{Ni}_2\text{O}_3/\text{TiO}_2\text{-xB}_x$ under visible irradiation, *J. Am. Chem. Soc.* 126 (2004) 4782–4783.
- [24] Z. Bian, T. Tachikawa, P. Zhang, M. Fujitsuka, T. Majima, Au/TiO_2 superstructure-based plasmonic photocatalysts exhibiting efficient charge separation and unprecedented activity, *J. Am. Chem. Soc.* 136 (2014) 458–465.
- [25] W. Zhao, Y. Sun, F.N. Castellano, Visible-light induced water detoxification catalyzed by PtII dye sensitized titania, *J. Am. Chem. Soc.* 130 (2008) 12566–12567.
- [26] B. Palanisamy, C.M. Babu, B. Sundaravel, S. Anandan, V. Murugesan, Sol-gel synthesis of mesoporous mixed $\text{Fe}_2\text{O}_3/\text{TiO}_2$ photocatalyst: application for degradation of 4-chlorophenol, *J. Hazard. Mater.* 252–253 (2013) 233–242.
- [27] X. Xiong, Y. Xu, Synergetic effect of Pt and borate on the TiO_2 -photocatalyzed degradation of phenol in water, *J. Phys. Chem. C* 120 (2016) 3906–3912.
- [28] G.S. Pozan, A. Kambur, Removal of 4-chlorophenol from wastewater: preparation, characterization and photocatalytic activity of alkaline earth oxide doped TiO_2 , *Appl. Catal. B Environ.* 129 (2013) 409–415.
- [29] J. Yuan, E. Wang, Y. Chen, W. Yang, J. Yao, Y. Cao, Doping mode, band structure and photocatalytic mechanism of B-N-codoped TiO_2 , *Appl. Surf. Sci.* 257 (2011) 7335–7342.
- [30] H.K.J. Sato, Y. Inoue, Photocatalytic activity for water decomposition of indates with octahedrally coordinated d^{10} configuration. II. Roles of geometric and electronic structures, *J. Phys. Chem. B* 107 (2003) 7970–7975.
- [31] I.D. Brown, D. Altermatt, Bond-valence parameters obtained from a systematic analysis of the inorganic crystal structure database, *Acta Cryst. B* 41 (1985) 244–247.
- [32] W. Melitz, J. Shen, A.C. Kummel, S. Lee, Kelvin probe force microscopy and its application, *Surf. Sci. Rep.* 66 (2011) 1–27.
- [33] V. Palermo, M. Palma, P. Samori, Electronic characterization of organic thin films by kelvin probe force microscopy, *Adv. Mater.* 18 (2006) 145–164.
- [34] J. Roncali, P. Leriche, P. Blanchard, Molecular materials for organic photovoltaics: small is beautiful, *Adv. Mater.* 26 (2014) 3821–3838.
- [35] L. Hu, D.-B. Li, L. Gao, H. Tan, C. Chen, K. Li, M. Li, J.-B. Han, H. Song, H. Liu, J. Tang, Graphene doping improved device performance of ZnMgO/PbS colloidal quantum dot photovoltaics, *Adv. Funct. Mater.* 26 (2016) 1899–1907.
- [36] S. Moniz, S.A. Shevlin, D. Martin, Z.X. Guo, J.W. Tang, Visible-light driven heterojunction photocatalysts for water splitting – a critical review, *Energy Environ. Sci.* 8 (2015) 731–759.
- [37] V. Palermo, G. Ridolfi, A.M. Talarico, L. Favaretto, G. Barbarella, N. Camaioni, P. Samori, A kelvin probe force microscopy study of the photogeneration of surface charges in all-thiophene photovoltaic blends, *Adv. Funct. Mater.* 17 (2007) 472–478.
- [38] B. Gao, L. Liu, J. Liu, F. Yang, Photocatalytic degradation of 2,4,6-tribromophenol over Fe-doped ZnIn_2S_4 : Stable activity and enhanced debromination, *Appl. Catal. B: Environ.* 129 (2013) 89–97.
- [39] X. Li, J. Fang, G. Liu, S. Zhang, B. Pan, J. Ma, Kinetics and efficiency of the hydrated electron-induced dehalogenation by the sulfite/UV process, *Water Res.* 62 (2014) 220–228.
- [40] T. Tachikawa, T. Ochi, Y. Kobori, Crystal-face-dependent charge dynamics on a BiVO_4 photocatalyst revealed by single-particle spectroelectrochemistry, *ACS Catal.* 6 (2016) 2250–2256.
- [41] Y. Guo, J. Li, Z. Gao, X. Zhu, Y. Liu, Z. Wei, W. Zhao, C. Sun, A simple and effective method for fabricating novel p–n heterojunction photocatalyst $\text{g-C}_3\text{N}_4/\text{Bi}_4\text{Ti}_3\text{O}_{12}$ and its photocatalytic performances, *Appl. Catal. B Environ.* 192 (2016) 57–71.
- [42] C. Tang, L. Liu, Y. Li, Z. Bian, Aerosol spray assisted assembly of TiO_2 mesocrystals into hierarchical hollow microspheres with enhanced photocatalytic performance, *Appl. Catal. B: Environ.* 201 (2017) 41–47.
- [43] T. Hirakawa, Y. Nosaka, Properties of O_2^{2-} and OH^- formed in TiO_2 aqueous suspensions by photocatalytic reaction and the influence of H_2O_2 and some ions, *Langmuir* 18 (2002) 3247–3254.
- [44] C.R. Bowen, H.A. Kim, P.M. Weaver, S. Dunn, Piezoelectric and ferroelectric materials and structures for energy harvesting applications, *Energy Environ. Sci.* 7 (2014) 25–44.